 Bull. Chem. Soc. Jpn., 76, 945–959 (2003)

Electronic and Magnetic Properties of Organic Conductors $(DMET)_2MBr_4$ (M = Fe, Ga)

Kengo Enomoto,* Jun-Ichi Yamaura,† Akira Miyazaki, and Toshiaki Enoki*

Department of Chemistry, Tokyo Institute of Technology, Ookayama, Meguro, Tokyo 152-8551

†Institute for Solid State Physics, University of Tokyo, Kashiwanoha 5-1-5, Kashiwa, Chiba 277-8581

(Received November 11, 2002)

$(DMET)_2MBr_4$ (M = Fe, Ga) are isostructural organic conductors whose crystal structure consists of an alternate stacking of quasi one-dimensional chain-based donor layers and anion square lattices. The resistivity, ESR, magnetic susceptibility, magnetization, and magnetoresistance of these salts were investigated in order to clarify the correlation between the electronic structure and the magnetism. The electronic structures of both salts are metallic down to T_{MI} ~40 K, below which a Mott insulating state is stabilized, accompanied by an SDW transition at T_{SDW} ~25 K. The $FeBr_4$ salt with Fe^{3+} ($S = 5/2$) localized spins undergoes an antiferromagnetic transition at $T_N = 3.7$ K. In the $FeBr_4$ salt, the magnetization curves, which show field-direction-dependent anomalies in addition to a spin-flop transition, are demonstrated to have a participation of donor π-electron spins in the magnetization processes. The field dependence of the magnetoresistances below T_N tracks faithfully that of the magnetization, where the donor π-electrons and Fe^{3+} d-electrons are responsible for the former and the latter, respectively. This clearly demonstrates the presence of the π–d interaction that plays an important role in the interplay between electron transport and magnetism.

Since the discovery of the first one-dimensional (1D) organic metal, TTF-TCNQ, organic molecular conductors composed of TTF derivatives have drawn much attention in solid state physics and chemistry. These π-electron systems form a large variety of electronic structures among the metallic state, charge density wave (CDW) state, spin density wave (SDW) state, Mott insulating state, and superconducting state. This diversity comes from competition between the transfer integral, the on-site Coulomb interaction, and the electron–phonon interaction in low-dimensional frames.[1,2] In order to elucidate the origin of these solid state properties, extensive studies have been carried out, mainly on two families of compounds. The first family is TMTSF (tetramethyltetraselenafulvalene) salts belonging to a quasi-1D electronic system, such as $(TMTSF)_2PF_6$, while the second one is BEDT-TTF (bis(ethylenedithio)tetrathiafulvalene) salts, which are featured with quasi-2D one. Despite the difference in the dimensionality of their electronic structures, the phase diagrams of these two typical organic metals and superconductors share similar features.

Besides the electronic properties, magnetism is another attractive subject in organic molecular conductors. For instance, the introduction of localized d-electrons into organic conductors provides new aspects in low-dimensional conducting systems. The localized d-electrons play a role of magnetism and are expected to interact with the π-electrons in low-dimensional organic conductors. Based on this viewpoint, there have been attractive interests in designing new organic conductors containing localized magnetic moments.[3–13] Quite recently, magnetic-field-induced superconductivity was found, in which interactions between conducting π-electrons and localized magnetic d-electrons (π-d interaction) played an important role.[12,13]

The aim of the present work is to study the interplay between the conducting π-electrons and the localized magnetic d-electrons in organic magnetic conductors. According to this motif, we employ DMET (4′,5′-dimethyl-4,5-(ethylenedithio)-1′,3′-diselena-1,3-dithiafulvalene)[14] as a donor molecule and MBr_4 (M = Fe, Ga) as counter anions, where the localized magnetic moments of Fe^{3+} ($S = 5/2$) ions are incorporated into the π-electron network of DMET. The $GaBr_4$ salt, which is composed of diamagnetic anions ($S = 0$), can be treated as a reference material to investigate the properties of π-electron carriers and to estimate the effect of the π-d interaction of the $FeBr_4$ salt.

DMET is an unsymmetrical donor regarded as a hybrid between TMTSF and BEDT-TTF (Fig. 1(a)). According to its hybrid nature, DMET compounds provide a large variety of properties arising from its wide range of dimensionalities from 1D to 2D nature. For example, DMET salts with octahedral anions, such as PF_6^-, form quasi-1D conductors and are semiconducting even at room temperature.[15] Salts with linear anions, such as $[Au(CN)_2]^-$, I_3^-, and $[AuBr_2]^-$, provide various electronic properties from insulating to superconducting.[16,17] Salts with tetrahedral anions, for example $(DMET)_2BF_4$ and $(DMET)_2ClO_4$, form the "double-column" structure, which has not been found either the TMTSF family or the BEDT-TTF family, where these DMET salts have two types of donor columns elongated along the *a* and *b*-axes of the crystal lattice.[18,19] These salts with tetrahedral anions undergo metal-insulator transitions at between 30 and 40 K, whose insulating states consist of multiple phases.[20] As the title compounds, $(DMET)_2MBr_4$ (M = Fe, Ga), contain tetrahedral anions, they are also expected to belong to the same group as to

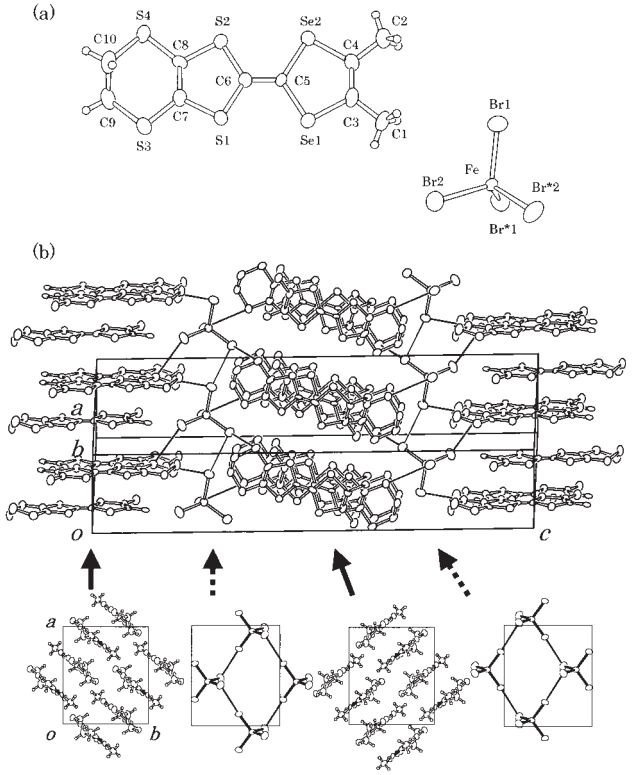

Fig. 1. (a) Molecular structures of the DMET donor and the $FeBr_4^-$ anion with the labeling of the atoms at room temperature. The atom labeling with asterisk indicates crystallographic equivalent atoms, which are plotted by symmetry operation $(1-x, y, -z+0.5)$. (b) The crystal structure of $(DMET)_2FeBr_4$. Cross sectional views of donor and anion layers are also drawn. Solid lines in the both figures denote close intermolecular Br···S and Br···Br contacts.

$(DMET)_2BF_4$, $(DMET)_2ClO_4$, which exhibit wealthy π-electron properties.[21,22]

We are interested not only in the properties of π-electron systems, but also in the interplay between the conduction π-electrons and the localized magnetic d-electrons. In the present paper, we report on the results of the crystal structure, the band structure, the electrical resistivities, ESR, the magnetic susceptibilities and the magnetoresistance in order to understand systematically the electronic and magnetic properties of $(DMET)_2MBr_4$ (M = Fe, Ga).

Experimental

Single crystals of $(DMET)_2FeBr_4$ and $(DMET)_2GaBr_4$ were prepared by the electrochemical oxidation of DMET (5–15 mg) in chlorobenzene (15 mL), using $(Bu_4N)FeBr_4$ or $(Bu_4N)GaBr_4$ (20–40 mg) as a supporting electrolyte, under an argon atmosphere at room temperature. A constant current of 0.25 μA was applied for 7–14 days. The typical size of the obtained plate-shaped crystals was $0.7 \times 0.7 \times 0.1$ mm^3 for both salts.

The crystal structures were determined using a Rigaku AFC-7R four-circle X-ray diffractometer with Mo Kα radiation at room temperature. The intensity data were collected in the range of $2\theta = 5$ to 55°, and the absorption effect was corrected empirically (ψ-scan method).[23] The reflections that satisfy $|F_o|^2 > 2\sigma(|F_o|^2)$ were used for further analysis. The structures were solved by direct methods, and refined on $|F|^2$ with a full-matrix least-squares method using SHELX programs.[24] Anisotropic temperature factors were used for all non-hydrogen atoms. The hydrogen atoms were placed at geometrically-calculated positions and refined isotropically. The crystallographic data and final *R*-factors are listed in Table 1. Crystallographic data have been deposited at the CCDC, 12 Union Road, Cambridge CB2 1EZ UK and copies can be obtained on request, free of charge, by quoting the publication citation and the deposition numbers 204409–204410. X-ray oscillation photographs were taken in the temperature range 16–300 K using a Weisenberg-type imaging plate (MAC Science DIP320) equipped with a closed-cycle helium refrigerator (DAIKIN Co. V202C5LZR) and monochromatic Mo Kα X-ray radiation supplied by a 15 kW-rotating anode. The single crystal was mounted with Apiezon-T grease on a sapphire rod attached to a copper cold finger of a closed-cycle refrigerator.

Table 1. Crystallographic Data of $(DMET)_2MBr_4$ (M = Fe, Ga)

	$(DMET)_2FeBr_4$	$(DMET)_2GaBr_4$
Chemical formula	$C_{20}H_{20}S_8Se_4FeBr_4$	$C_{20}H_{20}S_8Se_4GaBr_4$
Formula weight	1208.18	1222.04
Crystal system	Monoclinic	Monoclinic
Space group	$C2/c$	$C2/c$
a/Å	10.536(5)	10.541(13)
b/Å	9.183(2)	9.186(5)
c/Å	34.601(15)	34.583(14)
β/°	94.17(4)	94.12(6)
V/Å^3	3339(2)	3340(5)
Z	8	8
D_c/g·cm^{-3}	2.404	2.430
Radiation	Mo (Kα)	Mo (Kα)
Wavelength/Å	0.71069	0.71069
Temperature/K	298	298
Independent reflcns	2886	3263
Observed reflcns ($>2\sigma(I)$)	2157	2967
R, R_w	0.062, 0.155	0.10, 0.258

The transfer integrals between donor molecules and the energy band structure at room temperature were calculated based on the tight-binding approximation using the extended Hückel parameters[25] for the $FeBr_4$ salt.

The electrical resistivities for both salts were measured by a DC four-probe technique under ambient pressure in the temperature range of 1.5–300 K. The magnetic susceptibilities and magnetization curves were measured with a SQUID magnetometer (Quantum Design MPMS-7) in the temperature range of 1.8–300 K under a magnetic field of up to 7 T. The spin susceptibilities were obtained after subtraction of the Pascal diamagnetic contribution of $\chi_{dia} = -5.28$, and -5.26×10^{-4} emu/mol for the $FeBr_4$ and the $GaBr_4$ salts, respectively, from the observed susceptibilities.[26] ESR measurements for both salts were carried out with a single crystal, using an X-band ESR spectrometer (JEOL JES-TE200) with a He cryostat (Oxford ESR910) in the temperature range 3.5–300 K. A single crystal was mounted on a Teflon rod, and sealed in a sample tube with thermal exchange gas (He 15 Torr). The magnetoresistances for the $FeBr_4$ salt were measured using a 15-Tesla superconducting magnet (Oxford Instruments) in the temperature range of 1.6–4.2 K.

Table 2. Atomic Parameters of $(DMET)_2FeBr_4$ (see Fig. 1(a) for the atom indices)

Atom	x/a	y/b	z/c	U_{eq}/Å$^{2a)}$
Fe	0.5000	0.1846(2)	0.2500	0.0243(5)
Br1	0.32529(14)	0.03692(17)	0.26038(4)	0.0507(4)
Br2	0.54891(18)	0.32879(18)	0.30424(5)	0.0615(5)
Se1	0.44436(12)	0.22900(14)	0.46167(3)	0.0345(3)
Se2	0.26210(12)	−0.02386(13)	0.48561(3)	0.0332(3)
S1	0.5112(3)	0.2948(3)	0.55494(8)	0.0335(7)
S2	0.3407(3)	0.0627(3)	0.57741(8)	0.0329(7)
S3	0.5954(3)	0.3841(4)	0.63389(9)	0.0429(8)
S4	0.3889(4)	0.1040(4)	0.66148(9)	0.0420(8)
C1	0.3839(14)	0.1670(17)	0.3823(3)	0.046(3)
C2	0.2004(13)	−0.0900(16)	0.4057(4)	0.045(3)
C3	0.3574(12)	0.1186(14)	0.4219(3)	0.035(3)
C4	0.2809(12)	0.0097(12)	0.4323(3)	0.032(3)
C5	0.3750(11)	0.1273(12)	0.5020(3)	0.027(2)
C6	0.4058(11)	0.1589(12)	0.5400(3)	0.029(2)
C7	0.5023(12)	0.2666(12)	0.6043(3)	0.033(3)
C8	0.4215(12)	0.1600(12)	0.6148(3)	0.031(3)
C9	0.5860(15)	0.3019(16)	0.6803(4)	0.052(4)
C10	0.4496(16)	0.2615(15)	0.6892(4)	0.052(4)

a) Displacement parameter U_{eq} is defined on the basis of the following equation: $U_{eq} = (1/3)\sum_i \sum_j U_{ij} a_i^* a_j^* \mathbf{a}_i \mathbf{a}_j$.

Table 3. Bond Lengths and Angles of $(DMET)_2FeBr_4$ (see Fig. 1(a) for the atom indices)

Bond length/Å			
Fe1–Br2	2.323(2)	S3–C7	1.740(13)
Fe1–Br1	2.335(2)	S3–C9	1.784(14)
Se1–C5	1.872(10)	S4–C8	1.753(12)
Se1–C3	1.892(13)	S4–C10	1.825(15)
Se2–C5	1.888(11)	C1–C3	1.487(16)
Se2–C4	1.896(12)	C2–C4	1.513(18)
S1–C6	1.724(12)	C3–C4	1.349(18)
S1–C7	1.737(11)	C5–C6	1.363(15)
S2–C8	1.742(12)	C7–C8	1.364(16)
S2–C6	1.747(12)	C9–C10	1.54(2)
Bond angle/°			
Br1–Fe1–Br*1	108.97(12)	C2–C4–Se2	113.5(9)
Br1–Fe1–Br2	109.74(6)	C6–C5–Se1	122.3(9)
Br1–Fe1–Br*2	108.91(7)	C6–C5–Se2	123.2(8)
Br2–Fe1–Br*2	110.55(13)	Se1–C5–Se2	114.5(5)
C5–Se1–C3	94.6(5)	C5–C6–S1	123.1(9)
C5–Se2–C4	93.7(5)	C5–C6–S2	121.9(9)
C6–S1–C7	96.1(6)	S1–C6–S2	115.0(6)
C8–S2–C6	95.4(6)	C8–C7–S3	128.7(9)
C7–S3–C9	101.6(6)	C8–C7–S1	116.6(9)
C8–S4–C10	99.6(6)	S3–C7–S1	114.7(7)
C4–C3–C1	128.5(12)	C7–C8–S2	116.8(9)
C4–C3–Se1	118.1(9)	C7–C8–S4	128.6(9)
C1–C3–Se1	113.4(10)	S2–C8–S4	114.6(6)
C3–C4–C2	127.3(12)	C10–C9–S3	113.3(10)
C3–C4–Se2	119.1(9)	C9–C10–S4	112.5(10)

Results

Crystal Structure. In this section, we focus on the crystal structure of $(DMET)_2FeBr_4$, since that of the $GaBr_4$ salt was found to be isostructural, as shown in Table 1. The atomic coordinates with thermal parameters are summarized in Table 2 and the intramolecular distances and bond angles are given in Table 3, where the molecular structure and the atom indices are shown in Fig. 1(a). The crystal structure shown in Fig. 1(b) is characterized with an alternating stack of DMET donor π-electron conducting sheets and MBr_4 anion sheets. The unit cell contains eight DMET donor and four MBr_4 molecules. DMET donors are arranged in a face-to-face manner in the *ab*-plane to form a 2D sheet consisting of 1D backbones, while MBr_4 anions form a 2D deformed-square lattice in the *ab*-plane. For the $FeBr_4$ salt, the interaction network formed with Br···Br atomic contacts (3.883(3) Å) between adjacent $FeBr_4$ units is featured with a Fe^{3+} ($S = 5/2$) magnetic square lattice. Moreover, because the shortest inter-atomic distance between S and Br (3.764(4) Å) is comparable to the sum of the corresponding van der Waals distances (3.65 Å), interplane interactions with considerable strengths between the DMET donors and $FeBr_4$ anions are expected.

The donor molecules form columns, which are extended along the $a + b$ and $a - b$ directions on adjacent donor layers, as exhibited in Fig. 1(b) with cross-sectional views parallel to the *ab*-plane. Therefore, the crystal structure of this compound is featured by the "double-column" structure, similar to that of the BF_4 and ClO_4 salts.[18,19] However, the detailed situation of the donor stacking is somewhat different between this compound and the BF_4 and ClO_4 salts. A comparison of the donor arrangements shows that this compound has equivalent transfer integral networks between adjacent donor layers, whereas different types of donor networks feature the BF_4 and ClO_4 salts. The transfer integral network in the donor sheet in the *ab*-plane is shown in Fig. 2(a). An estimation of the transfer integrals with the extended Hückel method provides $a_1 = 34.35$, $a_2 = 32.20$, $p = 4.45$, $q = 4.44$, and $r = 3.16 \times 10^{-2}$ eV.[27] The intra-chain transfer integrals (a_1 and a_2) are almost equivalent ($a_1/a_2 = 1.07$) to the strengths, which are almost one order of magnitude larger than those of the inter-chain transfer integrals (p, q, and r; the side-by-side atomic contact origin). Figure 2(b) shows the band structure and the Fermi surfaces calculated with the tight-binding method. The result suggests the presence of quasi-2D semi-metallic features with small Fermi surfaces, where the 2:1 donor/anion ratio gives the 3/4-filled band structure.

Properties of π-electron Systems. First, we performed six-terminal-transport measurements on a sample at room temperature in order to obtain information about the *c*-axis/*ab*-plane resistivity anisotropy.[29] According to the analysis proposed by Busch et al.,[30] the anisotropy of the resistivity (ρ_c/ρ_{ab}) is obtained from the ratio V_{top}/V_{bot},

$$\sqrt{\frac{\rho_c}{\rho_{ab}}} \approx \frac{L}{\pi D} \operatorname{arccosh}\left(\frac{V_{top}}{V_{bot}}\right), \quad (1)$$

where V_{top}/V_{bot}, ρ_c, ρ_{ab}, L, and D denote the ratio of the top and bottom sides of the voltage signals, the *c*-axis ($I \parallel$inter-plane) resistivity, the *ab*-plane ($I \parallel$in-plane) resistivity, the length and the thickness of the sample, respectively. In the present case, V_{bot} was always under the detection limit of

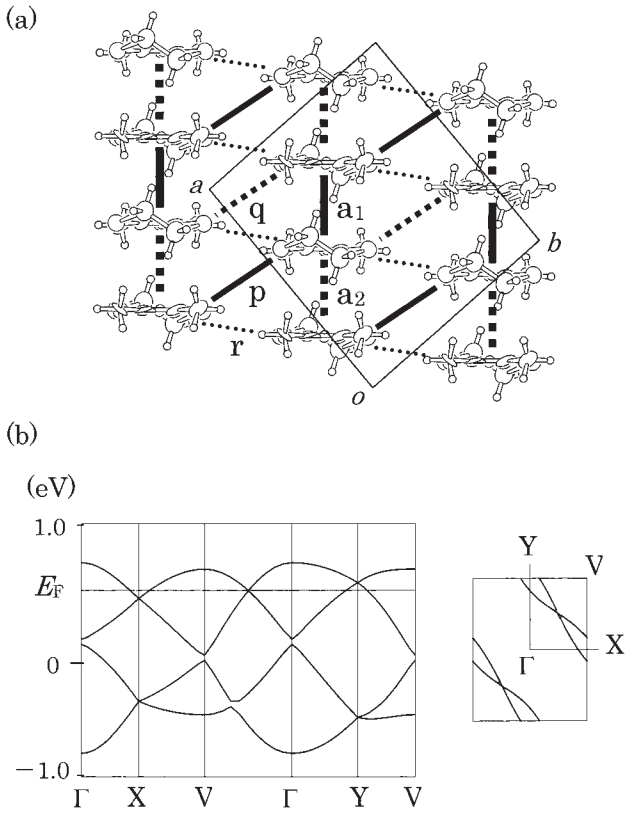

Fig. 2. (a) The arrangement of DMET donors projected on the *ab*-plane in $(DMET)_2FeBr_4$. One donor layer, where the π-electron conducting chains are extended along the $a+b$ direction, is focused. The inter-molecular transfer integrals are as follows; $a_1 = 34.35$, $a_2 = 32.20$, $p = 4.45$, $q = 4.44$, and $r = 3.16 \times 10^{-2}$ eV (Ref. 27). (b) Band structure and Fermi surfaces of $(DMET)_2FeBr_4$. Note that the Fermi surfaces on the donor layer adjacent to the layer shown in the figure are extended along another diagonal direction of the Brillouin zone since the donor chains are aligned along the $a+b$ and $a-b$ directions on adjacent donor layers.

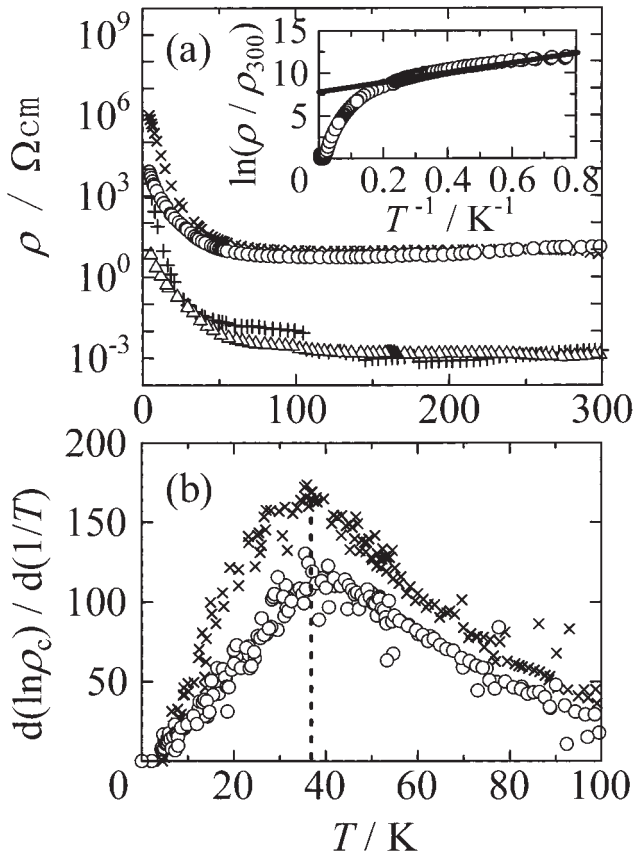

Fig. 3. (a) Temperature dependence of the electrical resistivities of $(DMET)_2FeBr_4$ ($\triangle$ and $\bigcirc$) and $(DMET)_2GaBr_4$ ($+$ and $\times$) measured in the *ab*-plane and along the *c*-axis at zero magnetic field, where in-plane (ρ_{ab}) and inter-plane (ρ_c) resistivities are denoted by $\triangle$, $+$ and $\bigcirc$, $\times$, respectively. Inset shows $\ln\rho$ vs T^{-1} plot of $(DMET)_2FeBr_4$. A solid line represents the resistivity calculated with the mean energy gap of 1.04×10^{-3} eV in the temperature range 1.5–5 K. (b) Numerical derivatives of the Arrhenius plot of ρ_c, $d(\log \rho_c)/d(1/T)$, calculated from the data in (a) for $(DMET)_2FeBr_4$ ($\bigcirc$) and $(DMET)_2GaBr_4$ ($\times$). The vertical dotted line denotes the temperature where the derivatives have maximum values.

our instrument, suggesting that the anisotropy (ρ_c/ρ_{ab}) is at least over 300. This large anisotropy indicates that the geometry, where the current terminals and voltage terminals were simply attached on the both surfaces, is appropriate for the *c*-axis ($I \parallel$inter-plane) resistivity measurements. Although this geometry includes a component of ρ_{ab} at a point of analysis, it has been commonly utilized in measurements.

The temperature dependence of the electrical resistivities for both salts was measured by the DC four-probe technique in the *ab*-plane (ρ_{ab}) and along the *c*-axis (ρ_c), as shown in Fig. 3(a). These salts are metallic around room temperature with $\rho_c \sim 10\ \Omega$ cm for the inter-plane direction and with $\rho_{ab} \sim 0.001\ \Omega$ cm for the in-plane direction. This large anisotropy ($\rho_c/\rho_{ab} \sim 10^4$) indicates that the probability of π-electron hopping events for the inter-plane direction is very small. The *ab*-plane resistivity shows an almost similar temperature dependence to that of the *c*-axis resistivity, although it often faces resistance jumps, which makes features of the phase transition ambiguous. These resistance jumps are caused by thermal-contraction-induced stress on the samples. In the present paper, the temperature dependence of the *c*-axis resistivities is used for the purpose of discussion due to its better quality. With decreasing temperature, the resistivities decrease down to about 100 K, and then increase semiconductively. To show details about the change in the behavior, the numerical derivative of the Arrhenius plot of ρ_c is presented in Fig. 3(b). One peak is clearly seen at around $\sim$40 K in this plot. Here, it should be noted that both salts are considered to have the same properties of π-electron carriers based on the temperature dependence of the resistivity behavior, which is consistent with the same crystal structure.

The temperature dependence of the magnetic susceptibility is shown in Fig. 4 for non-magnetic $(DMET)_2GaBr_4$ in an applied field ($B = 1$ T) parallel to the *ab*-plane, where single crystals are crystallographically aligned in the measurement. This salt, where the spin susceptibility comes only from the

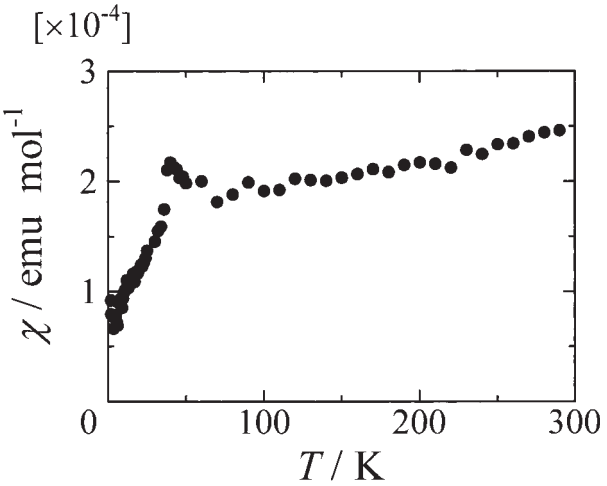

Fig. 4. Temperature dependence of the magnetic susceptibility of the polycrystalline $(DMET)_2GaBr_4$ sample measured at $B = 1$ T parallel to the *ab*-plane, where the *c*-axes of all the crystals are aligned to the same direction, the *a*-axes being randomly oriented.

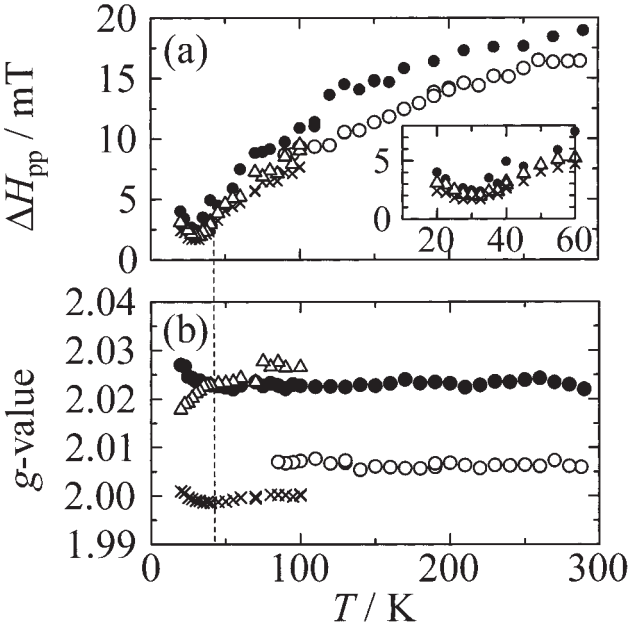

Fig. 5. Temperature dependence of the peak-to-peak ESR line width ΔH_{pp} (a) and the *g*-value (b) in the magnetic field along the $a \pm b$ direction (○, △, and ×) and the *c*-axis direction (●) for $(DMET)_2GaBr_4$. The inset in (a) shows the detailed behavior of ΔH_{pp} at low temperatures. The ESR signal along the $a \pm b$ direction is split to two Lorentzians below ~100 K. Symbols △ and × represent the results of the two Lorentzian fittings. The results of the two analyses (single Lorentzian and two Lorentzians) are shown in the temperature range 80–100 K. The vertical dotted line denotes the temperature (~40 K), where the *g*-value and the resistivity show anomalies.

π-electron part, shows a weakly temperature-dependent Pauli paramagnetic behavior at around room temperature. The absolute value of the susceptibility is in the same range as that of other metallic compounds in the DMET family.[21] The susceptibility slightly decreases with lowering the temperature down to 40 K, at which point a slight hump appears. It then rapidly decreases below this temperature, having a shoulder at around 25 K. The susceptibility has a finite value even at $T = 0$ K, which is ~30% of that at 40 K. The abrupt decrease in the susceptibility at 40 K, in addition to the Arrhenius plot's anomaly in the resistivity, indicates that a metal-insulator (MI) transition occurs at T_{MI} ~40 K. In consideration of the mechanism of this MI transition, the possibility of CDW or spin-Peierls (SP) transitions is ruled out, since no difference appears in the X-ray oscillation photographs between above and enough below T_{MI} (figure not shown).

For elucidating what is the ground state of donor π-electrons, we measured the ESR spectra of $(DMET)_2GaBr_4$. In this connection, a comparison of the spin susceptibility (χ_{spin}) and the ESR line width (ΔH_{pp}) to those of $(DMET)_2BF_4$ and $(DMET)_2ClO_4$ is useful,[21] because these salts have similar "double-column" structures.[18,19] The observed ESR signals of these related salts show a Dysonian line shape at lower temperatures. The asymmetry parameter becomes maximum at the temperature where these salts have a maximum conductivity. However, we always obtain Lorentzian peaks for $(DMET)_2GaBr_4$ over the whole temperature range when the DMET conducting donor layers are perpendicular to the electric field of microwaves. On the other hand, when the DMET conducting donor layers are parallel to the electric field, we obtain Dysonian peaks below room temperature ($T > 100$ K). These findings suggest metallic features of the donor conducting sheets for this salt. In the later discussion, for simplicity, we employ the ESR results only in the region where the ESR signal is Lorentzian.

At room temperature, the ESR absorption signals are single Lorentzian for both in-plane and *c*-axis directions (ΔH_{pp} ~16 mT with g ~2.006 along the $a \pm b$ directions and ΔH_{pp} ~19 mT with g ~2.023 for the *c*-axis direction). It is difficult to exactly determine whether the field is applied along the $a + b$ or the $a - b$ direction due to a difficulty to discriminate between these two directions based on the crystal appearance for the *ab*-plane measurement. Below 100 K, the signal is split to two Lorentzian-type lines for the $a \pm b$ directions, whereas it remains a single Lorentzian peak in the whole temperature range for the *c*-axis direction. The two Lorentzian-type line shapes are analyzed by the superposition of two Lorentzian fittings which do not interfere with each other. These ESR features are associated with the "double-column" stacking nature of the donors, as discussed later. Figures 5(a) and (b) show the temperature dependence of the peak-to-peak line widths (ΔH_{pp}) and the *g*-values. For both the $a \pm b$ and the *c*-axis directions, ΔH_{pp} decreases with a gentle convex curvature with decreasing the temperature, and is abruptly broadened below about 25 K, while it is split below ~100 K in the $a \pm b$ direction, as can be seen in the figure. The *g*-value for the *c*-axis direction is almost constant in the temperature range of 40–300 K, and slightly increases below 40 K (~T_{MI}). Along the $a \pm b$ directions, the *g*-value is also almost constant in the temperature range of 100–300 K. However, the splitting of the *g*-values clearly appears below 100 K, which can be explained by a "double-column" structure in the donor system.

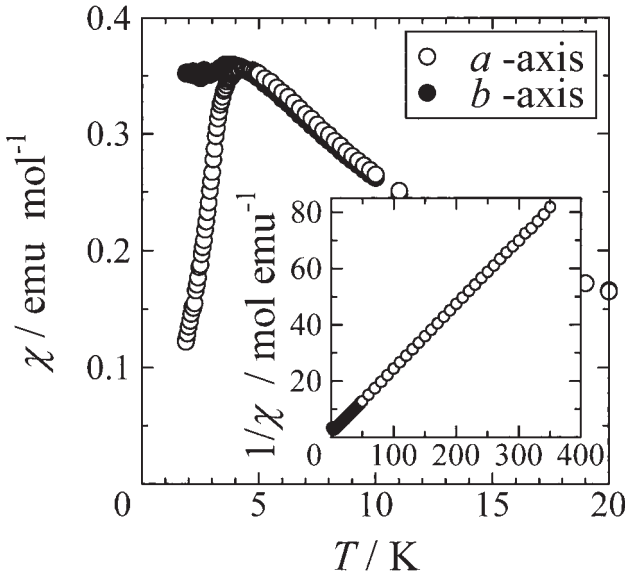

Fig. 6. Temperature dependence of the magnetic susceptibility of $(DMET)_2FeBr_4$ in the applied field of $B = 1$ T parallel to the a- (○) and b-axes (●). The inset shows the reciprocal susceptibility with the field parallel to the ab-plane.

The two split g-values are considered to correspond to those normal to the donor molecular plane ($g_1 \sim 2.000$) and along the short side direction ($g_2 \sim 2.024$), consistent with the donor configurations in the crystal structure.[1] These g-values show a temperature-independent behavior in the temperature range of 40–100 K, and then finally begin to shift to the opposite directions to each other, resulting in a decrease in the difference of the split g-values below 40 K.

Properties of π-d Interaction System: $(DMET)_2FeBr_4$. Figure 6 shows the temperature dependence of the magnetic susceptibilities of $(DMET)_2FeBr_4$ in an applied field ($B = 1$ T) parallel to the a- and b-axes, whose directions were determined from an X-ray analysis before the susceptibility measurement. The reciprocal susceptibility vs the temperature is also plotted in the figure for a field applied in the ab-plane. The susceptibilities show a Curie–Weiss behavior in the temperature range of 20–300 K, where the Curie constant is $C = 4.4$ emu·K/mol and the Weiss temperature is $\theta = -6$ K. The observed value of the Curie constant indicates that the magnetism is governed mainly by Fe^{3+} ($S = 5/2$) d-electrons. The Fe^{3+} d-electron spins undergo a 3D antiferromagnetic ordering at $T_N = 3.7$ K. The susceptibility in the field parallel to the a-axis approaches zero as the temperature decreases, showing that the easy-axis is oriented to the a-axis. This direction corresponds to the longer diagonal of the Fe^{3+} magnetic deformed-square lattice. The presence of the antiferromagnetic transition evidences the important role of the interlayer interactions between the Fe^{3+} layers, because no long-range order exists at a finite temperature in pure 2D Heisenberg antiferromagnets, taking into account that the Fe^{3+} ($S = 5/2$) state has isotropic spins.[31] The absence of a short-range order effect in the susceptibility, which is confirmed by an excellent linearity in the $1/\chi$ vs T plot, even in the vicinity of T_N, also proves that the interlayer interactions between the Fe^{3+} layers are strong enough to give a 3D long-range ordering.

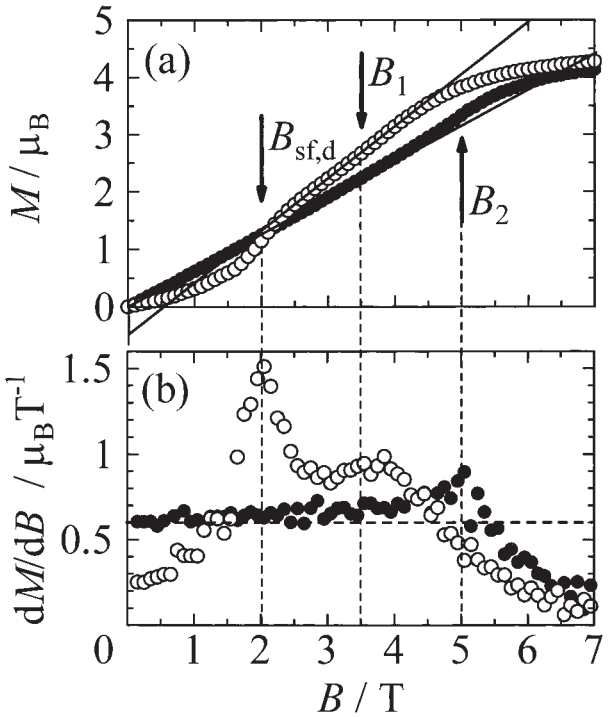

Fig. 7. (a) Magnetization curves of $(DMET)_2FeBr_4$ measured at $T = 1.8$ K in the field parallel to the a- (○) and b-axes (●). A spin-flop transition is observed at $B_{sf,d} = 2$ T when the field is applied parallel to the a-axis. The magnetization curves are saturated above $B_{sat} \sim 6.5$ T. The solid lines for the a- and b-axes represent the extrapolations of the linear part of the magnetization curves. (b) The numerical derivatives as a function of applied field, i.e. the field dependence of the susceptibility. B_1 and B_2 indicate the fields, at which the susceptibilities take peaks in the a- and b-axis directions, respectively.

Magnetization curves in the field parallel to the a- and b-axes at 1.8 K are shown in Fig. 7(a). In the magnetization curves, a spin-flop transition is observed at $B_{sf,d} = 2.0$ T when an external field is applied parallel to the a-axis. It should be noted that the easy-axis ($B \parallel a$) magnetization curve of the Fe^{3+} spins is larger than the hard-axis ($B \parallel b$) magnetization curve above the spin-flop field $B_{sf,d}$. In addition to this anomaly, the easy-axis magnetization curve is extrapolated to a negative value at $B = 0$, and the hard-axis magnetization curve has a shoulder at around $B \sim 5$ T. These features are far from the behavior of ordinary antiferromagnets. Here, one can see the anomalies more clearly on the field dependence of the susceptibilities, as shown in Fig. 7(b). In the a-axis direction, the first and second anomalies emerge at $B_{sf,d} = 2.0$ T and $B_1 = 3.5$ T, respectively, while one anomaly exists at $B_2 = 5.0$ T in the b-axis direction. These anomalies at B_1 and B_2 cannot be explained in terms of only the Fe^{3+} ($S = 5/2$) spins, which strongly suggest that the DMET donor π-electron spins importantly participate in the magnetism.

In order to confirm the contribution of the donor π-electron spins in the magnetism, the ESR spectra were next measured for $(DMET)_2FeBr_4$. The line width is very large ($\Delta H_{pp} \sim 70$ mT for the ab-plane direction and $\Delta H_{pp} \sim 100$ mT for the c-

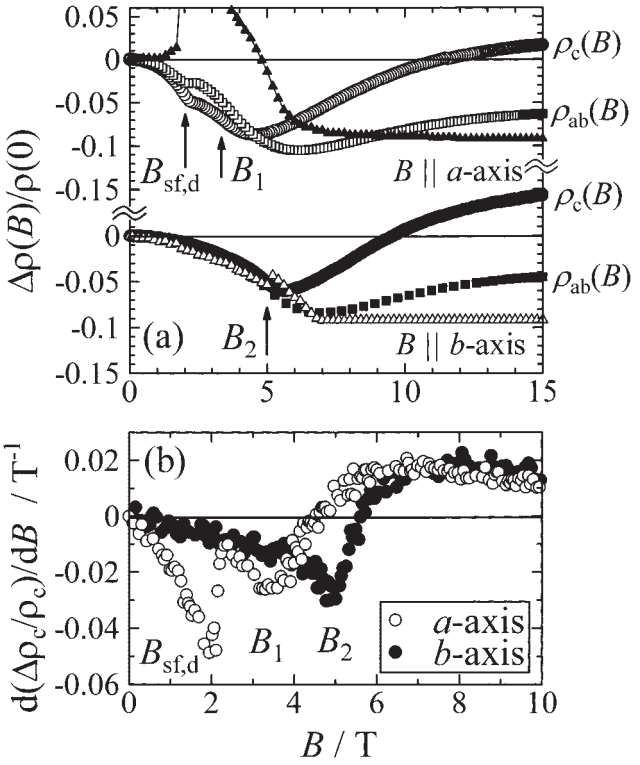

Fig. 8. (a) Field dependence of $\Delta\rho_{ab}(B)/\rho_{ab}(0)$ (□ and ■) and $\Delta\rho_c(B)/\rho_c(0)$ (○ and ●) measured at $T = 1.6$ K. The calculated results are also shown for the a-axis (▲) and the b-axis (△) ($p \sim 1$; see text for the definition of p in Section Discussion). (b) The numerical derivatives of the inter-plane magnetoresistance as a function of applied field. The applied field is parallel to the a-axis (○) and the b-axis (●). Three anomalies are clearly detected at $B_{sf,d}$, B_1, and B_2.

axis direction) even at room temperature, and increases with decreasing the temperature. The g-values are estimated to be 2.04 and 2.06 for the ab-plane and c-axis directions, respectively, at room temperature. We also tried to take antiferromagnetic resonance, and found an observation difficulty due to the magnitudes of the exchange interaction and the magnetic anisotropy, which do not meet the experimental condition in the X-band ESR region.

The ab-plane/c-axis (in-plane/inter-plane) anisotropy of the magnetoresistances were measured for $(DMET)_2FeBr_4$ in the field parallel to the a- and b-axes. A six-terminal technique was employed in the measurements, which have already been explained. Figure 8(a) represents the field dependence of the in-plane and inter-plane magnetoresistances measured at $T = 1.6$ K ($<T_N$), which correspond to $\Delta\rho_{ab}(B)/\rho_{ab}(0) = \{\rho_{ab}(B) - \rho_{ab}(0)\}/\rho_{ab}(0)$ and $\Delta\rho_c(B)/\rho_c(0) = \{\rho_c(B) - \rho_c(0)\}/\rho_c(0)$, respectively. In the field along the Fe^{3+} spin easy-axis direction ($B \parallel a$), both the in-plane ($\Delta\rho_{ab}(B)/\rho_{ab}(0)$) and the inter-plane ($\Delta\rho_c(B)/\rho_c(0)$) magnetoresistances show anomalous features at $B_{sf,d}$ and B_1. On the other hand, an anomalous discontinuity appears at B_2 for the hard-axis direction ($B \parallel b$), although it is necessary to take the derivative of the magnetoresistance for confirming it, as we will see later. A different behavior between the in-plane and the inter-plane magnetoresistances appears in the high-field regime, where $\Delta\rho_{ab}(B)/\rho_{ab}(0)$ has a negative value up to 15 T with a minimum appearing at around 6–7 T, while $\Delta\rho_c(B)/\rho_c(0)$ has positive values above $B \sim 10$–12 T. The numerical derivatives of the inter-plane magnetoresistance as a function of the applied field are shown in Fig. 8(b). Similar to the field dependence of the susceptibilities, an anomaly corresponding to the spin-flop field is observed as the first peak at $B_{sf,d} = 2.0$ T, and the other anomaly as the second peak at $B_1 = 3.5$ T for the a-axis direction, while an anomaly as the first peak appears at $B_2 = 5.0$ T for the b-axis direction. It is worth noting here that there is an excellent correspondence between the magnetization and the magnetoresistance, where the former and the latter are governed by the d-electrons and π-electrons, respectively, demonstrating the important role of the π-d interaction.

Here, we estimate the inter-plane carrier hopping frequency ($\omega_\perp$) from the anisotropy of ρ_{ab}/ρ_c, where $\omega_\perp$ is defined as the inverse of the time during which one electron hopping event takes place between adjacent donor layers. In general, the inter-plane resistivity (ρ_c) can be expressed in terms of a combination of the in-plane relaxation process and the inter-plane electron hopping in a layered 2D system.[32] Namely, an electron staying on one layer, which is subjected to the in-plane carrier scattering process with relaxation time $\tau_\parallel$, happens to hop to the adjacent layer in the inter-plane carrier transport event with the assistance of phonons or defects. Therefore, ρ_{ab} and ρ_c are expressed as

$$\rho_{ab} \propto 1/\tau_\parallel, \tag{2}$$

$$\rho_c \propto \frac{1}{\omega_\perp \tau_{coll}}, \tag{3}$$

where $\tau_\parallel$ and τ_{coll} are the relaxation time of the in-plane carrier scattering and the collision time related to $\tau_\parallel$, respectively. In other words, $\tau_\parallel$ becomes identical to τ_{coll} by neglecting the forward scattering factor $(1 - \cos\theta)$. From Eqs. 2 and 3, the field dependence of the inter-plane hopping frequency can be estimated as

$$\frac{\Delta\omega_\perp(B)}{\omega_\perp(0)} = \frac{\omega_\perp(B) - \omega_\perp(0)}{\omega_\perp(0)} \approx \left(\frac{\rho_{ab}(B)}{\rho_{ab}(0)} \Big/ \frac{\rho_c(B)}{\rho_c(0)} - 1\right), \tag{4}$$

where $\rho_{ab}(B)/\rho_{ab}(0)$ and $\rho_c(B)/\rho_c(0)$ are the ratios of the in-plane and the inter-plane magnetoresistances, respectively. The field-dependent term of the inter-plane hopping frequency, $\Delta\omega_\perp(B)/\omega_\perp(0)$, calculated from Eq. 4, is shown in Fig. 9. In the Fe^{3+} spin easy-axis direction ($B \parallel a$), $\Delta\omega_\perp(B)/\omega_\perp(0)$ increases with a positive curvature up to $B_{sf,d} = 2.0$ T. After a discontinuous change at around $B_{sf,d}$, it shows a gradual decrease up to B_1, and then steeply decreases with a positive curvature, where the sign is changed to negative above ca. 5 T. In the Fe^{3+} spin hard-axis direction ($B \parallel b$), it always has a negative value with a discontinuous change at $B_2 = 5.0$ T, at which point the magnetization has an anomaly, as discussed before. The absolute values of $\Delta\omega_\perp(B)/\omega_\perp(0)$ tend to be saturated to the same value as the field goes above ca. 8 T, irrespective of the direction of the applied field.

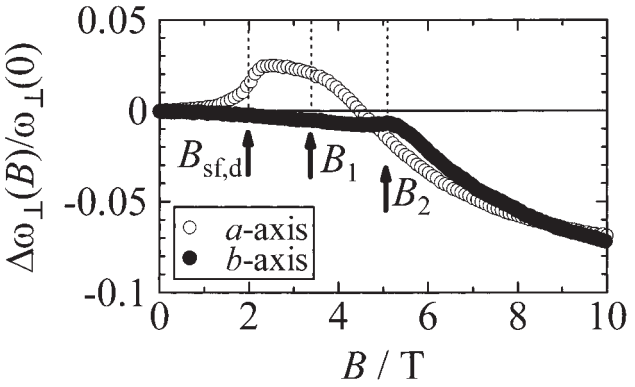

Fig. 9. The field dependence of the inter-plane hopping frequency ($\Delta\omega_\perp(B)/\omega_\perp(0)$). The applied magnetic field is parallel to the *a*-axis (○) and the *b*-axis (●). The vertical dotted lines with arrows correspond to $B_{sf,d}$, B_1, and B_2.

Finally, it should be noted that a previous paper[33] dealing with the same compound, $(DMET)_2FeBr_4$, suggested an MI transition at 200 K, which contradicts the present results with $T_{MI} = 40$ K. Although the difference in the properties has not been clearly understood, where a minority of the samples take 200 K as the MI transition temperature, all of the experimental results in the present work, which have been done with a vast number of samples, show the same properties with a transition temperature at 40 K. The problem on samples with $T_{MI} = 200$ K remains to be clarified in the future.

Discussion

Electronic Structure of π-electron Systems. First, we discuss the inter-donor-layer interaction based on the temperature dependence of the ESR spectra of $(DMET)_2GaBr_4$ by focusing on the origin of two split peaks in the field along the $a \pm b$ direction. Judging from the crystal structure, donor molecules form quasi-1D donor chains extending along the $a + b$ and $a - b$ directions on adjacent two donor layers, while the long axes of the donor molecules are nearly parallel to the *c*-axis, irrespective of the directions of the donor chains. Therefore, two kinds of donor columns on the adjacent layers are generally nonequivalent as viewed from the direction perpendicular to the *c*-axis, being expected to give two ESR peaks unless the inter-donor-layer interaction is strong. Actually, two Lorentzian peaks appear in the field parallel to the conduction plane below ~100 K, at which the resistivity behavior is switched from a decreasing trend to an increasing trend upon lowering of the temperature. The *g*-values of the two peaks correspond to the direction of the molecular short side and the direction normal to the donor molecular plane in the field along the $a \pm b$ direction. The spin susceptibilities (χ_{spin}), derived from the ESR absorption intensity, have almost the same values for both split-Lorentzian peaks, which also indicate that these ESR signals are a consequence of the "double-column" structure. The experimental findings that show a correlation between the ESR peak splitting and the change in the resistivity trend suggest an important role of the inter-donor-layer π-electron hopping in the ESR motional narrowing phenomenon in the metallic regime above ca. 100 K. Namely, motional narrowing effect makes a single Lorentzian peak in the temperature range down to ca. 100 K, while showing a decrease in the inter-plane hopping rate, which is evidenced by an increase in the inter-plane resistivity, degrades the motional narrowing effect below this temperature, giving two split peaks. The inter-plane hopping frequency ($\omega_\perp$) is estimated from the difference in the *g*-values, $\Delta g = g_A - g_B \sim 2.4 \times 10^{-2}$, between the two adjacent donor layers (A and B). Namely, if the inter-plane hopping frequency is large enough ($\omega_\perp > \Delta g \mu_B H/\hbar$), the ESR absorption signals, which are attributed to adjacent donor layers, become coalescent. The experimental results indicate that the inter-plane hopping energy ($\hbar\omega_\perp$) become lower than $\sim 4.7 \times 10^{-5}$ eV below ca. 100 K, the value of which is about two or three-orders of magnitude smaller than the intra-layer transfer integrals, suggesting 2D features in the π-electronic system.

Here, it is worth comparing the behavior of $(DMET)_2GaBr_4$ with that of its all-sulfur version $(EDTDM)_2GaBr_4$, where the structures of both salts are isostructural.[5] Similar to the result for the present compound, the ESR signal of the EDTDM salt appears as two split peaks, even at room temperature, in the field along the $a \pm b$ direction, while a single peak appears in the field parallel to the *c*-axis. The line width shows a remarkable difference between the two salts. The DMET salt containing selenium atoms gives a broad ΔH_{pp} ($\Delta H_{pp} = 19$ mT for the *c*-axis at room temperature), in contrast to a sharp line width of the EDTDM salt ($\Delta H_{pp} = 0.7$ mT for the same direction), suggesting a large contribution of the spin-orbit interaction. However, the most important difference is produced by changes in the transfer integral and the on-site Coulomb repulsion energy (*U*) as a result of the substitution of chalcogen atoms; that is, the substitution of Se atoms with S atoms decreases the transfer integral, whereas the on-site Coulomb interaction is elevated by this substitution. The decrease in the transfer integral between the adjacent donor layers plays an important role in the motional narrowing mechanism in addition to the decrease in the intra-chain transfer integral. Accordingly, the electronic structure, which is more extended in $(DMET)_2GaBr_4$ than that in $(EDTDM)_2GaBr_4$, makes π-electron carriers more mobile, contributing to the motional narrowing effect more efficiently. This situation is quite similar to the difference between the TMTSF and the TMTTF families, where the salts having large t/U in the former, such as $(TMTSF)_2PF_6$, behave as being metallic down to ~10 K, while those with small t/U in the latter, such as $(TMTTF)_2PF_6$, behave as being semiconductive below room temperature.[34,35]

Next, we discuss the behavior of the π-electron carriers and the origin of the MI transition in $(DMET)_2GaBr_4$. In the metallic regime down to T_{MI} ~40 K, the ESR line width decreases upon lowering of the temperature. The ESR line width in a metallic system is governed by the spin-lattice relaxation process as the consequence of a motional narrowing effect in general, where the phonon-assisted relaxation mechanism plays an important role. In this case, according to the Elliott mechanism,[36] the line width (ΔH_{pp}) is given by

$$\Delta H_{pp} \sim a \frac{(\Delta g)^2}{\tau_\parallel}, \tag{5}$$

where Δg is the *g*-shift from the free-electron value, and is a

measure of the spin-orbit coupling, $\tau_\parallel$ is the relaxation time of carriers and a ($\approx$1) is a numerical factor. The importance of the phonon-assisted mechanism in the spin-lattice relaxation process, in which Eq. 5 is at work, is confirmed by the same decreasing trend in both the resistivity and ΔH_{pp} upon lowering the temperature in the temperature range above ca. 100 K, while taking into account that the resistivity is inversely proportional to $\tau_\parallel$. Below ca. 100 K, the resistivity and ΔH_{pp} lose their common trend in the temperature dependence; that is, the resistivity starts increasing, while the donor π-electron spins become independent from each other between the adjacent donor layers in the ESR signal, though decreasing trend still hold in ΔH_{pp}. These experimental findings suggest that the donor π-electronic system becomes more 2D as a consequence of a deceleration of the inter-plane hopping frequency in the temperature regime below ca. 100 K in comparison with that above ca. 100 K. The increase in the resistivity at temperatures well above T_{MI} ~40 K upon lowering of the temperature proves that low-dimensionality-inherited fluctuations seriously affect the electron-transport properties as a precursor of the MI transition.

The MI transition shows anomalous features, which are different from that in ordinary low-dimensional organic conductors. Here, we summarize what happens in the vicinity of the MI transition. At T_{MI} ~40 K, the resistivity shows an anomaly, while the spin susceptibility takes a discontinuous drop accompanied by shifts of the g-values. In addition to the MI transition, a second anomaly appears at 25 K, suggesting successive MI transition features. Namely, the susceptibility shows a hump at 25 K, and then has a finite value even at $T = 0$ K. Moreover, the ESR line width becomes broadened at around 25 K.

The transition at 25 K can be explained in terms of an SDW transition. Actually, the susceptibility, being small with a finite value even at $T = 0$ K, indicates that an antiferromagnetic or SDW state is stabilized for the π-electron insulating ground state. Moreover, the abrupt broadening of ΔH_{pp} just above 25 K is suggestive of a precursor of an antiferromagnetic ordering, and indicates that an SDW state is stabilized below 25 K ($\sim T_{SDW}$).

In the meantime, understanding the MI transition at T_{MI} ~40 K is rather difficult. For characterizing the MI transition, there are two important clues: the absence of a structural modification and the contribution of the magnetic degree of freedom. The possibility of a CDW or SP transition is ruled out from the absence of any structural modifications, as we have already discussed. In contrast, the contribution of magnetism reminds us of Mott or SDW transition as candidates, taking into account that the present compound is subjected to the influence of strong electron correlations ($U > 4t$). The g-value shift accompanied by a moderate decrease in the susceptibility below T_{MI} proves the development of a magnetic short-range order. Eventually, it is likely that the state between T_{SDW} and T_{MI} is characterized as a Mott insulator, where localized magnetic moments generated below T_{MI} in the low-dimensional donor π-electron system are fluctuating under the influence of a strong intra-chain exchange interaction.

Here, it is worth noting that $(DMET)_2BF_4$ and $(DMET)_2ClO_4$, also forming "double-column" structures, have similar multi-transition features, where the details remain unsolved.[20–22] The experimental findings in the present salts are expected to give clues for understanding the transition features.

In the present section, the discussion is devoted to $(DMET)_2GaBr_4$. However, it is reasonable to assume that $(DMET)_2FeBr_4$ has the same properties of π-electron carriers, taking into account the same crystal structure and the features of the resistivities for both salts (Fig. 3), although the localized Fe^{3+} spins work to give a modification in the π-electronic system.

π-d Interaction in $(DMET)_2FeBr_4$. In this section, we discuss the origin of the correlation between the Fe^{3+} ($S = 5/2$) localized spins and the donor conduction π-electrons in $(DMET)_2FeBr_4$ based on the crystal structure, susceptibility, magnetization, and magnetoresistance. There are two kinds of players in the magnetism of $(DMET)_2FeBr_4$: the donor π-electrons and Fe^{3+} d-electrons. Here, the donor π-electrons are affected by the internal magnetic field from Fe^{3+} spins, since each donor layer is sandwiched by 2D deformed-square lattice layers of Fe^{3+} localized spins, as shown in Fig. 1(b). Below T_{SDW} (= 25 K), the donor π-electrons fall into the SDW state, where the localized spins generated in the donor system are considered to be spatially ordered (we assume that $(DMET)_2FeBr_4$ has the same SDW transition temperature to $(DMET)_2GaBr_4$). The Fe^{3+} spins are antiferromagnetically ordered below $T_N = 3.7$ K.

First, we discuss the magnetic structure of the donor-Fe^{3+} spin composite system in the ordered state below T_N. For simplicity, a four-fold periodicity in the SDW state is assumed along the donor chains, since the electronic state is featured with the 3/4 filled state, although no information is available for the spatial distribution of localized magnetic moments.

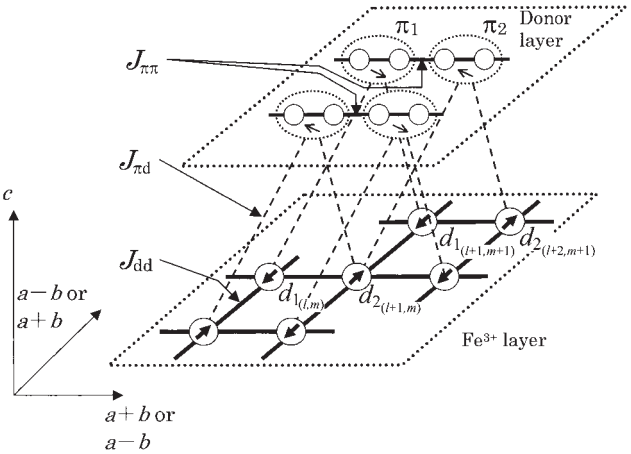

Fig. 10. The model of magnetic structure of $(DMET)_2FeBr_4$. A dotted circle denote a two-donor unit, to which one localized magnetic moment is allotted. Dashed lines represent exchange interaction $J_{\pi d}$ between a donor spin and an anion spin. Inter-π-electron spin and inter-Fe^{3+} spin interactions are defined as $J_{\pi\pi}$ and J_{dd}, respectively. π_i and d_i ($i = 1, 2$) represent the sublattices for the donor and Fe^{3+} spins, respectively. (l, m) represents a lattice point.

Namely, we place one donor spin at every two-donor unit, as shown in Fig. 10. In the unit cell that involves two Fe^{3+} layers and two donor layers, there are four Fe^{3+} and four π-electron sublattices in the magnetic structure. The involvement of all sublattices in the calculation brings us complexity and ambiguity, which cannot be overcome due to too many parameters for achieving the most stable magnetic structure. Therefore, we employ half of the sublattices by neglecting the difference in the adjacent donor layers, as shown in Fig. 10, with four sublattices (π_i and d_i ($i = 1, 2$)) for the donor and Fe^{3+} layers, respectively. The Fe^{3+} spins form an antiferromagnetic arrangement with two-fold periodicity along the direction of the donor-chain below T_N. Thus, the magnetic structure is governed by three kinds of antiferromagnetic exchange interactions (J_{dd}, $J_{\pi d}$, and $J_{\pi\pi}$), which are the inter-Fe^{3+} spin interaction, the interaction between the Fe^{3+} and the donor π-electron spins, and the inter-π-electron spin interaction, respectively. The numbers of nearest neighbor sites are $z_{dd} = 4$ and $z_{\pi\pi} = 2$ for J_{dd} and $J_{\pi\pi}$, respectively, where the interchain interaction is assumed to be neglected in the donor π-electron system, since it is more than one order of magnitude smaller than $J_{\pi\pi}$. (Note that J is proportional to the square of the transfer integral (t).) Focusing on the interaction network of $J_{\pi d}$, each π-electron spin has four neighbors of Fe^{3+} spins ($z_{\pi d} = 4$) located on two adjacent anion layers. The experimental results on the magnetization and magnetoresistance remind us the importance of $J_{\pi d}$ in the magnetic system.

In addition to the exchange interactions, the magnetic anisotropies for both the Fe^{3+} and the π-electron spins must be involved in the calculation, since the spin-flop transitions take place in the Fe^{3+} and the π-electron spins. Namely, the anomaly observed at B_2 in the b-axis direction is assumed to be assigned to the spin-flop transition (denoted as $B_{sf,\pi}$) of the π-electron spins (see Fig. 7(a)). The assumption can be reasonably understood, taking into account that a spin-flop transition is also observed in the SDW state of other organic low-dimensional electronic systems.[37] Concerning the magnitude of $B_{sf,\pi}$, which is about one order of magnitude larger than that of the other organic systems, the exchange interaction between the Fe^{3+} and π-electron spins should be taken into consideration. In fact, $B_{sf,\pi}$ increases correlatively with that of $J_{\pi d}$ in the present calculation, which evidences the contribution of $J_{\pi d}$.

We define the magnetic anisotropy ($K_{u\pi}$) for the donor π-electron spins, which is oriented to the b-axis for reproducing the π-electron spin-flop transition at $B_{sf,\pi}$ ($= B_2$) $\sim$5 T. This means that the π-electron spin easy-axis is considered to be perpendicular to the magnetic anisotropy of the Fe^{3+} spins, K_{ud} ($\| a$). Here, the origins of the magnetic anisotropy should be commented for the Fe^{3+} and π-electron spins. In general, there are three origins of magnetic anisotropy: the dipole-dipole interaction, the single-ion anisotropy, and the anisotropic exchange interaction. However, it is difficult to uniquely assign a specific origin for understanding the magnetic anisotropies of Fe^{3+} and π-electron spins. In other words, these three origins are considered to be involved in determining the magnetic anisotropies. The fact that the π-electron is not well localized on a single donor molecule in the SDW state also makes the situation complicated. Therefore, in the calculation, the directions of the magnetic anisotropies for the Fe^{3+} and π-electron spins are considered to be given *a priori* from the experimental results, without any further consideration.

In order to find the most stable magnetic structure, we calculate the magnetic energy at $T = 0$ K while changing the applied field based on a simple model, as derived in APPENDIX. A calculation requires the following adjustable parameters: the absolute values and the directions of the magnetic moments for the Fe^{3+} d-electron and the π-electron spins located on the four sublattices. The directions of the magnetic moments are given to be the spin angles with respect to the a-axis direction in the ab-plane, θ_{d_i} and θ_{π_i} for two Fe^{3+} and two π-spin sublattices ($i = 1, 2$), respectively. The absolute value of the Fe^{3+} spin is given to be $S_{d_i} = 5/2$ for the high spin state. Since the typical SDW in the organic low-dimensional systems, such as the TMTSF family, has small magnetic moments in the range of $\mu \approx 0.1\ \mu_B$,[38,39] we assume here that the π-electron spin (s_{π_i}) has a similar value. It is difficult to accurately estimate the magnitudes of the exchange interactions ($J_{\pi d}$, $J_{\pi\pi}$) and the magnetic anisotropy ($K_{u\pi}$) from the experimental results, since certain ambiguity remains in the magnitude of the magnetic moments of the π-electron spins. Here, we assume $J_{\pi d} = -0.2$ K, $J_{\pi\pi} = -13.5$ K, and $K_{u\pi} = 0.4$ K under the assumption of $\mu \sim 0.15\ \mu_B$, which are selected to reproduce the experimental results of the magnetization curves. The parameters of J_{dd} and K_{ud} are estimated to be $J_{dd} \approx -0.2$ K and $K_{ud} \approx 1.3$ K directly from the observed parameters (T_N, C, and $B_{sf,d}$) in the molecular-field approximation. The calculated results are shown in Fig. 11 for the magnetization curves in the field applied parallel to the a- and b-axis directions. The calculation of the magnetization curves at $T = 0$ K well reproduces the two features in the experimental results. First, the Fe^{3+} spin easy-axis ($B \| a$) magnetization curve is beyond the hard-axis ($B \| b$) magnetization curve above the spin-flop field ($B_{sf,d}$). Second, the

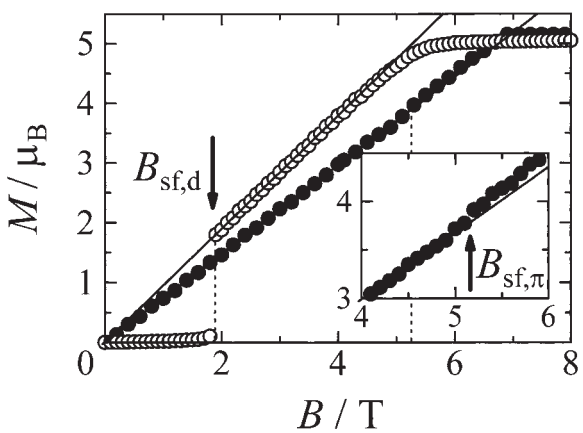

Fig. 11. Calculated magnetization curves at $T = 0$ K in the a- (○) and the b-axis (●) directions. The inset shows the detailed behavior around $\sim$5 T in the Fe^{3+} hard axis direction ($B \| b$), where a weak anomaly of π-electron spins appear as a spin-flop transition of the π-electron spins at $B_{sf,\pi}$ $\sim$5.2 T. The solid line represents the linear extrapolation from the data at low fields below 5 T. An arrow denotes the field, at which the magnetization deviates from the linear extrapolation.

Fe^{3+} spin hard-axis ($B \parallel b$) magnetization curve has a shoulder at around $B \sim 5.2$ T, i.e., the π-electron spin-flop transition ($B_{sf,\pi}$). There are two other features which are not reproduced in the calculation: the weak anomaly at $B_1 \sim 3.5$ T and the negative extrapolated value to $B = 0$ T for the a-axis magnetization. These failures are considered to be attributed to the assumption of the four sublattices model, in which the difference between the donor chain directions on adjacent donor layers is neglected. In addition, the two-donors-based π-electron spin structure with the four-fold periodicity in the model might affect the calculated results, since the SDW state in the actual system, which remains unspecified, can have another periodicity with a modified amplitude, depending on the feature of the Fermi surface.

Here, it is worth noting the difference in the magnetism between $(DMET)_2FeBr_4$ and λ-$(BETS)_2FeCl_4$. From the above calculation, the contribution of the π-d interaction ($-2J_{\pi d}s_\pi S_d$) is about one order of magnitude smaller than that of the direct inter-Fe^{3+} spin interaction ($-2J_{dd}S_dS_d$) in $(DMET)_2FeBr_4$, suggesting that the magnetic structure is governed by a direct interaction in the Fe^{3+} magnetic lattice.[28] This means that the magnetic effect of the Fe^{3+} spin system gives a moderate perturbation on the electron transport of the π-electron system with no serious influence in the π-electronic state, as discussed next. In contrast, λ-$(BETS)_2FeCl_4$ has a π-d interaction energy with its strength being comparable to that of the direct inter-Fe^{3+} spin interaction, the large modification of the π-electronic state being produced as reported previously.[9–13]

The next task is to explain the electron transport properties based on the magnetic structure model. Since the 1D donor chains lie along the direction of the alignment of the Fe^{3+} spins spanned by J_{dd}, where the Fe^{3+} and π-electron spins have the same periodicity, the localized donor spins are antiferromagnetically coupled with the Fe^{3+} spins to gain stabilization energy, which is governed by $J_{\pi d}$ (Fig. 10). In this situation, the magnitude of the π-electron SDW energy-gap (ΔE) is enhanced by the antiferromagnetic periodic potential of the Fe^{3+} spins, which results in a high resistivity below T_N at $B = 0$ T. The resistivity jump is clearly detected at T_N under high pressure in this compound,[40] even though it is difficult to detect the anomaly of the resistivity vs temperature plot around T_N at ambient pressure because of the high resistivity. This result suggests that the electronic system is sufficiently influenced by the antiferromagnetic exchange interaction ($J_{\pi d}$). In the next two sections, we discuss the behavior of the in-plane magnetoresistance ($\Delta\rho_{ab}(B)/\rho_{ab}(0)$) and the inter-plane carrier transport ($\Delta\omega_\perp(B)/\omega_\perp(0)$) based on the magnetic structure model, as discussed above.

1. In-plane Magnetoresistance: Here, we discuss the in-plane π-electron transport based on the model of the magnetic structure, where the Fe^{3+} localized spins and donor π-electron spins participate with a mutual interaction ($J_{\pi d}$), as explained in Fig. 12(a). The magnetoresistance has different features in the three field regimes: low field ($B \sim 0$), intermediate field ($0 < B \sim B_{sf,d} < B_{sat}$, B_{sat}; saturation field of the Fe^{3+} spins) and high field ($B > B_{sat}$), in relation to the changes in the Fe^{3+} magnetic structure. We describe the semi-quantitative analysis based on the magnetic-structure model.

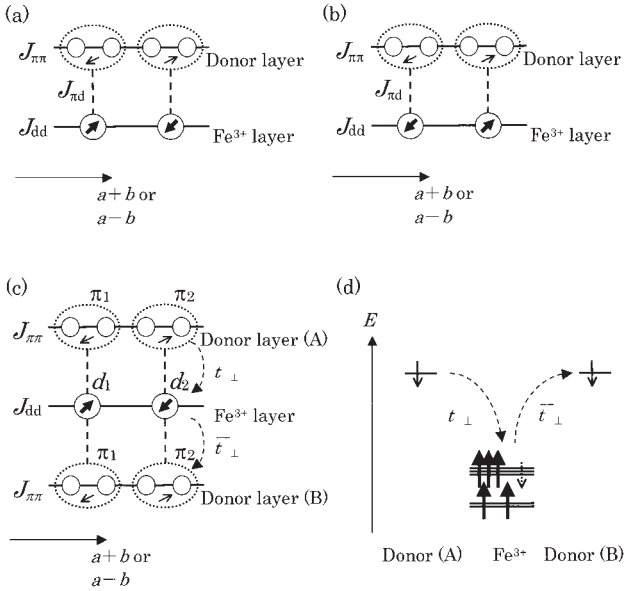

Fig. 12. The spin arrangements of antiparallel (a) and parallel (b) configurations between the donor and Fe^{3+} spins, where the fractions of the antiparallel and parallel configurations are exaggerated, respectively. (c) Scheme of the inter-plane electron hopping. $t_\perp$ is the transfer interaction between the donor and Fe^{3+} layers, while $\overline{t_\perp}$ is the average of transfer interaction $t_\perp$. π_i and d_i ($i = 1, 2$) are the sublattices of the Fe^{3+} and π-electron spins, respectively. (d) Electron transfer process between donor and Fe^{3+} states, where the Pauli principle governs the hopping event.

The SDW state of π-electrons is stabilized by $J_{\pi d}$, which makes the π-electron spins antiferromagnetically coupled with the Fe^{3+} spins, as shown in Fig. 12(a), where the fraction of the antiparallel configuration is exaggerated. In the actual $(DMET)_2FeBr_4$, where the π-electron spin easy-axis is almost perpendicular to the Fe^{3+} spin easy-axis, the fraction of the antiparallel configuration is only a minor contribution. The antiferromagnetic periodic potential of the Fe^{3+} spins is regarded as being the perturbation energy which works to enhance the π-electron SDW energy-gap. The energy gain originating from the antiferromagnetic coupling between the π-electron spins and the Fe^{3+} d-electron spins, which corresponds to the increase in the SDW gap, is given by the difference in the energies from the state given in Fig. 12(a) ($E_{(a)}$) to the state where the antiferromagnetic arrangement is absent in the Fe^{3+} magnetic lattice. The energy in the latter is approximately expressed as $(E_{(a)} + E_{(b)})/2$, where $E_{(b)}$ is the magnetic energy corresponding to the state shown in Fig. 12(b). Therefore, the increase in the SDW gap associated with the antiferromagnetic potential of the Fe^{3+} spin is given by Eq. 6, where $z_{\pi d}$, S_{d_i}, and s_{π_i} are the number of nearest neighbors connected by $J_{\pi d}$, the spin operators of Fe^{3+} and π-electrons, respectively (see APPENDIX); p is the proportional constant connecting between $\Delta E_{\pi d}(B)$ and the energy difference, representing the effectiveness of the magnetic energy change to the electron-transport process. Here, we neglect the minor changes happening in the donor π-electron spin chains and the Fe^{3+} layers, in which $J_{\pi\pi}$ and J_{dd} work, respectively, in

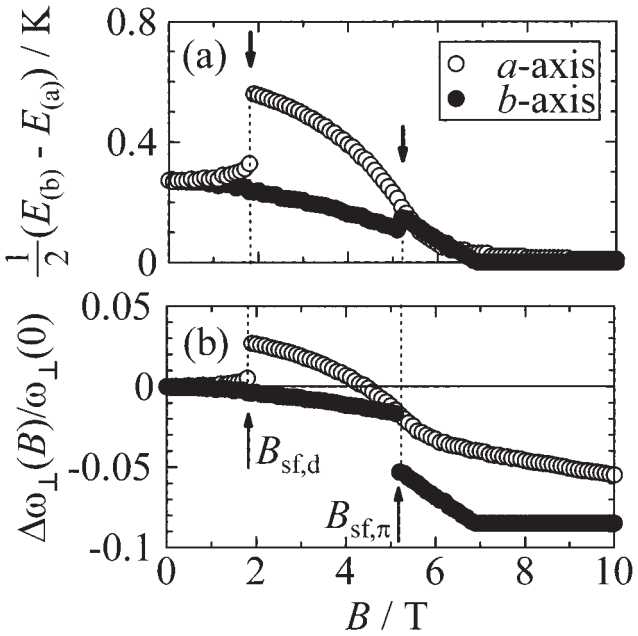

Fig. 13. (a) Calculation results of the perturbation energy $(E_{(b)} - E_{(a)})/2$ in the in-plane carrier transport. See text for the definitions of $E_{(a)}$ and $E_{(b)}$. (b) Calculation results of the field dependence of the inter-plane hopping frequency $\Delta\omega_\perp(B)/\omega_\perp(0)$. The arrows denote the fields ($B_{sf,d} \sim 2$ T and $B_{sf,\pi} \sim 5$ T) which give discontinuous changes at spin-flop transitions of Fe^{3+} and donor spins, respectively.

the calculation.

$$\Delta E_{\pi d}(B) \approx p\left[\frac{E_{(a)} + E_{(b)}}{2} - E_{(a)}\right] = \frac{1}{2}p[E_{(b)} - E_{(a)}]$$
$$\approx -pJ_{\pi d}z_{\pi d}\sum_{i=1}^{2} S_{d_i}s_{\pi_i}\cos(\theta_{d_i}(b) - \theta_{\pi_i}(b))$$
$$+ pJ_{\pi d}z_{\pi d}\sum_{i=1}^{2} S_{d_i}s_{\pi_i}\cos(\theta_{d_i}(a) - \theta_{\pi_i}(a)), \quad (6)$$

Figure 13(a) represents the calculation results obtained by Eq. 6. In the low-field regime ($B \sim 0$), $(E_{(b)} - E_{(a)})/2$ has a finite value in the range of 0.27 K, irrespective of the field direction. In the intermediate regime ($0 < B < B_{sat}$), it tends to increase with a discontinuous upsurge at $B_{sf,d}$ in the a-axis direction, followed by a continuous decrease up to the saturation field of the Fe^{3+} spins. For the b-axis direction, it shows a monotonical decrease up to the saturation field of the Fe^{3+} spins with a small upturn at the spin-flop transition ($B_{sf,\pi}$) of the donor π-electron spins. Finally, at fields higher than B_{sat}, $(E_{(b)} - E_{(a)})/2$ disappears irrespective of the field direction, in which the π-electron transport process is not subject to the influence of the π-d interaction-related perturbation energy due to the ferromagnetic alignment of Fe^{3+} spins. Therefore, the in-plane resistivity in the field can be expressed in terms of $\Delta E_{\pi d}(B)$,

$$\rho_{ab}(B,T) \approx \rho_0 \exp\left(\frac{E_0 + \Delta E_{\pi d}(B)}{2k_B T}\right)$$
$$= \rho_0 \exp\left[\frac{(E_0 + \Delta E_{\pi d}(0)) - (\Delta E_{\pi d}(0) - \Delta E_{\pi d}(B))}{2k_B T}\right], \quad (7)$$

where E_0 is the SDW energy-gap in the absence of a Fe^{3+} internal field, which corresponds to that for $(DMET)_2GaBr_4$. $(E_0 + \Delta E_{\pi d}(0))$ is the energy gap for $(DMET)_2FeBr_4$ at $B = 0$ T, which is estimated to be 1.04×10^{-3} eV from the temperature dependence of the resistivity in the temperature range of 1.5–5 K. Taking into account that the energy difference $(\Delta E_{\pi d}(0) - \Delta E_{\pi d}(B_{sat}))$ is in the range of 0.27 K ($p \sim 1$), the π–d interaction ($J_{\pi d}$) gives a contribution of $\sim 10\%$ at most to the total resistivity at the temperature, where the magnetotransport is investigated. The value of p is employed from the fitting to the experimental result, as will be described below. The calculated results with Eq. 7 are shown in Fig. 8(a) compared with the experimental results. Eq. 7 reproduces magnetoresistance traces semi-quantitatively, especially for the case with $B \parallel b$ in the field range ($B < B_{sat} \sim 6$ T), in which Eq. 7 is applicable. Here, it should be noted that the contribution of the orbital degree of freedom does not seriously affect the calculated results because the magnetoresistance of nonmagnetic $(DMET)_2GaBr_4$, which has only the contribution of the π-electrons, is less than $\sim 3\%$ of the observed magnetoresistance.[40] A large discrepancy in the vicinity of $B_{sf,d}$ for the case with $B \parallel a$ is considered to come from the oversimplified model which we employ for the magnetic structure. The model involves four sublattices, neglecting the difference in the donor chains placed on the adjacent layers. In the actual system, the participation of spins at the eight sublattices works to reduce the change in $\Delta E_{\pi d}(B)$, giving rise to the observed moderate change at $B_{sf,d}$ with a decreasing trend of the magnetoresistance upon an elevation of the field. The disagreement in the high fields above B_{sat} is associated with a lack of consideration on the field dependence of the unperturbed SDW energy-gap (E_0) and the orbital effect. The application of the field in the conducting plane is considered to increase the energy of the π-electron system, giving a high resistivity as the orbital effect.[41]

2. Inter-plane Carrier Transport: In the inter-plane carrier transport, the inter-plane hopping frequency ($\omega_\perp$) plays a key role, where the inter-plane resistivity is given in Eq. 3, as we have already discussed. The observed field dependence of the hopping frequency ($\Delta\omega_\perp(B)/\omega_\perp(0)$) is given in Fig. 9 for the field directions parallel to the a- and b-axes. In contrast to the in-plane magnetoresistance, the π-electrons are affected directly by the state of localized d-electrons in the inter-plane hopping mechanism, since the Fe^{3+} magnetic layer makes a bridge between the adjacent donor layers, as shown in Fig. 12(c). The electron hopping event crucially depends on the mutual angle between the π-electron and the Fe^{3+} d-electron spins due to the Pauli principle. Taking into account that Fe^{3+} high spin state is the half-filled $3d^5$ state, as shown in Fig. 12(d), with only the π-electron having a spin antiparallel to the Fe^{3+} spin being allowed to be transferred to the Fe^{3+} d-state. In contrast, the transport of a π-electron having parallel

spin is completely forbidden. Accordingly, the angular dependence of the transfer interaction is proportional to $(1 - \cos(\theta_{d_i} - \theta_{\pi_i}))$. Note that the π-electron spin at π_i is coupled with the Fe^{3+} spin at d_i by $J_{\pi d}$. The angular dependence discussed here is valid only in the case that the arrangement of the donor π-electron spins has a periodicity same to that of the Fe^{3+} d-electron spins, which we assume in the magnetic structure model having the four-fold periodicity shown in Fig. 12(c). In the general case, where the periodicity of the π-electron spins is described by the wave number (Q), the angular dependence of the transfer interaction ($t_\perp$) should be modified, as expressed by the following equation due to the coexistence of the fractions of up- and down-spins:

$$t_{\perp_i} \approx t_{0_i} - t_{1_i} \cos(\theta_{d_i} - \theta_{\pi_i}), \quad (i = 1, 2), \tag{8}$$

where t_{0_i} and t_{1_i} are the spin-independent and spin-dependent transfer interactions along the c-axis, respectively. An inter-plane electron hopping event involves two processes, as explained by Figs. 12(c) and (d). As shown in Fig. 12(d), the first one is the electron-transfer process from one donor layer (A) to the Fe^{3+} site, while the electron, occupying the Fe^{3+} d-level with its spin aligned antiparallel to the spins of the five remaining d-electrons, is transferred to the adjacent donor layer (B) in the second process. In the first process, the Pauli principle plays an important role in the easiness of the electron transfer, which is subjected to the angular dependence of the transfer interaction given in Eq. 8. On the other hand, the second process from the Fe^{3+} site to the donor layer (B) does not have a serious angular dependence, since the SDW state on the donor layer (B) is described in terms of the combination of the wave functions of the up- and down-spins. The electron being transferred to the donor layer (B) can find a vacancy for its accommodation regardless of the spin orientation. Therefore, the inter-plane hopping frequency is described phenomenologically by

$$\omega_\perp(B) \propto t_\perp \overline{t_\perp}, \tag{9}$$

where $\overline{t_\perp}$ is the average of the transfer interaction in the second process. The calculation of the hopping frequency as a function of the applied field is carried out using Eqs. 8, 9 and the spin angles obtained from Eq. 14. Here, we estimate the value of the spin-dependent/spin-independent ratio as $t_1/t_0 \approx 0.1$ in this calculation. The calculation result is shown in Fig. 13(b), which can reproduce the experimental results shown in Fig. 9, as follows:

1) In the low-field regime ($0 < B < B_{sf,\pi}$), a discontinuous upsurge in $\Delta\omega_\perp(B)/\omega_\perp(0)$ is clearly detected around $B_{sf,d}$ in the a-axis direction due to the spin-flop transition of the Fe^{3+} spins. Since the π-electron spins are influenced directly by the state of the Fe^{3+} spins, the anomaly at $B_{sf,d}$ is the consequence of a significant change in the magnetic energy for the a-axis direction. Above $B_{sf,d}$, $\Delta\omega_\perp(B)/\omega_\perp(0)$ decreases upon an elevation of the field, changes sign and tends to decrease its slope above $B_{sf,\pi}$. On the other hand, $\Delta\omega_\perp(B)/\omega_\perp(0)$ shows no significant change below ca. $B_{sf,\pi}$ for the b-axis direction, since the mutual angle between the Fe^{3+} spins has a continuous change towards saturation. At the spin-flop transition of the π-electron spins at $B_{sf,\pi}$, $\Delta\omega_\perp(B)/\omega_\perp(0)$ shows a discontinuous decrease.

2) In the high-field regime ($B > B_{sf,\pi}$), a vigorous decrease of $\Delta\omega_\perp(B)/\omega_\perp(0)$ occurs when the field exceeds $B_{sf,\pi}$ for the b-axis direction. Here, we discuss the mechanism of this vigorous decrease while taking into account the π-electron spin-flop transition for the b-axis direction. Below $B_{sf,\pi}$, the SDW state is well stabilized, the numbers of up- and down-spins being almost equivalent. However, the numbers of spins become inequivalent above the donor spin-flop field ($B_{sf,\pi}$), where the fraction of spins oriented to the field direction overwhelms that oriented antiparallel to the field direction. In this regime, since almost all of the Fe^{3+} spins are ferromagnetically arranged to the field direction, the number of electrons that can be transferred to the Fe^{3+} d-state becomes reduced due to the Pauli principle upon an elevation of the field, resulting in a slow down of the inter-plane hopping process (Fig. 12(d)). This situation provides the mechanism where the inter-plane hopping frequency has a discontinuous reduction at $B_{sf,\pi} = 5.2$ T, and also explains the behavior of the magnetization, which has an anomaly at $B_{sf,\pi}$ in the spin hard-axis ($B \parallel b$). Moreover, these results also meet the situation that the donor spin easy-axis is oriented along to the b-axis.

Conclusion

We investigated the electronic and magnetic properties of $(DMET)_2MBr_4$ (M = Fe, Ga) by means of crystal structure analysis as well as resistivity, ESR, magnetic susceptibility, magnetization, and magnetoresistance studies. These two isostructural organic conductors are composed of an alternate stack of quasi-1D donor π-electron conducting sheets and square-lattice anion sheets. In the $FeBr_4$ salt, the inter-plane exchange interactions with considerable strengths between the DMET π-electron carriers and the localized magnetic moments of the $FeBr_4$ anions are expected due to the presence of short intermolecular Br···S contacts. The resistivities of both salts behave as being metallic at around room temperature, and metal-insulator transitions take place at $T_{MI} \sim 40$ K, below which localized magnetic moments of the π-electrons are produced. The finite value of the π-electron spin susceptibility at $T = 0$ and the abrupt broadening of ΔH_{pp} at around 25 K indicate the onset of an SDW transition at $T_{SDW} \sim 25$ K, which is well below T_{MI}.

The $FeBr_4$ salt has a square lattice of Fe^{3+} ($S = 5/2$) spins, which undergo an antiferromagnetic transition at $T_N = 3.7$ K. The magnetization curves below T_N, which show an anomalous behavior in addition to a spin-flop transition of the Fe^{3+} spins, suggest the important role of donor π-electron spins stabilized in the SDW state. The magnetoresistance faithfully tracks the magnetization behavior, demonstrating the important contribution of the π-d interaction. The correlation between the π-electron transport and the magnetism of the localized d-electron spins can be understood based on the formation of SDW in the π-electron system that interacts with the Fe^{3+} d-electron spin system. The exchange interaction between the π- and d-electrons influences the π-electron transport process, giving a correlated behavior between the magneto-transport and the magnetization.

The semi-quantitative calculation based on a simple magnetic structure model with Fe^{3+} and π-electron spins, where the π–d interaction is taken into account, can reproduce the ex-

perimental results of the magnetization curves and the magnetoresistance. This proves that the inter-plane interaction between the conduction π-electron carriers and the localized magnetic d-electrons (π-d interaction) plays an important role in the magneto-transport properties and the magnetism, although several minor issues remain unsolved. A more elaborated model will be required for a comprehensive understanding of the correlation between the electron magneto-transport properties and the magnetism.

$(DMET)_2FeBr_4$, which is classified in the moderate π–d interaction regime, gives a new type of magnetic organic conductor with an interesting interplay between the electron transport and the magnetism, in contrast to λ-$(BETS)_2FeCl_4$, which has a strong π-d interaction.

The authors would like to express their sincere thanks to Professor Ko Sugihara, Professor Hidekazu Tanaka, Professor Hidetoshi Fukuyama, and Dr. Chisa Hotta for fruitful discussion. This work was supported by a Grant-in-Aid for Scientific Research on Priority Area (No. 12046231) from the Ministry of Education, Science, Sports and Culture.

Appendix: Magnetic Structure at $T = 0$ K

The exchange interaction energy per unit cell is given by the spin operators of the Fe^{3+} and π-electrons, $\mathbf{S}_l$ and $\mathbf{s}_m$ by

$$\begin{aligned} E_{\mathrm{ex}} &= \frac{1}{N_{\mathrm{u}}}\Bigg[-2J_{\mathrm{dd}} \sum_{\substack{\langle l,m\rangle \\ l\in d_1, m\in d_2}} \mathbf{S}_l\mathbf{S}_m \\ &\quad - 2J_{\pi\mathrm{d}} \sum_{i=1}^{2} \sum_{\substack{\langle l,m\rangle \\ l\in d_i, m\in \pi_i}} \mathbf{S}_l\mathbf{s}_m - 2J_{\pi\pi} \sum_{\substack{\langle l,m\rangle \\ l\in \pi_1, m\in \pi_2}} \mathbf{s}_l\mathbf{s}_m\Bigg] \\ &= -2J_{\mathrm{dd}}z_{\mathrm{dd}}\mathrm{S}_{\mathrm{d}_1}\mathrm{S}_{\mathrm{d}_2}\cos(\theta_{\mathrm{d}_1} - \theta_{\mathrm{d}_2}) \\ &\quad - 2J_{\pi\mathrm{d}}z_{\pi\mathrm{d}} \sum_{i=1}^{2} \mathrm{S}_{\mathrm{d}_i}\mathrm{s}_{\pi_i}\cos(\theta_{\mathrm{d}_i} - \theta_{\pi_i}) \\ &\quad - 2J_{\pi\pi}z_{\pi\pi}\mathrm{s}_{\pi_1}\mathrm{s}_{\pi_2}\cos(\theta_{\pi_1} - \theta_{\pi_2}), \end{aligned} \tag{10}$$

where N_{u} is the number of unit cells, z_{dd}, $z_{\pi\mathrm{d}}$, and $z_{\pi\pi}$ are the numbers of nearest neighbors connected by J_{dd}, $J_{\pi\mathrm{d}}$, and $J_{\pi\pi}$, respectively, and $\mathrm{S}_{\mathrm{d}_i}$ and s_{π_i} ($i = 1$ or 2) represent Fe^{3+} ($S = 5/2$) and π-electron spins on sublattices d_i and π_i, respectively.

The anisotropy energy per unit cell is given by

$$\begin{aligned} E_{\mathrm{anis}} &= K_{u\mathrm{d}}\{\sin^2(\theta_{\mathrm{d}_1}) + \sin^2(\theta_{\mathrm{d}_2})\} \\ &\quad + K_{u\pi}\{\sin^2(\psi_\pi - \theta_{\pi_1}) + \sin^2(\psi_\pi - \theta_{\pi_2})\}, \end{aligned} \tag{11}$$

where $K_{u\mathrm{d}}$ and $K_{u\pi}$ are the anisotropy energies of the Fe^{3+} and π-electron spins per mole, respectively, and ψ_π represents the angle between the π-electron spin easy-axis and the a-axis.

The Zeeman energy per unit cell is given by

$$E_{\mathrm{field}} = -g\mu_{\mathrm{B}}BM, \tag{12}$$

where the magnetization M is described as

$$\begin{aligned} M &= \{S_{\mathrm{d}_1}\cos(\theta_{\mathrm{B}} - \theta_{\mathrm{d}_1}) + S_{\mathrm{d}_2}\cos(\theta_{\mathrm{B}} - \theta_{\mathrm{d}_2})\} \\ &\quad + \{s_{\pi_1}\cos(\theta_{\mathrm{B}} - \theta_{\pi_1}) + s_{\pi_2}\cos(\theta_{\mathrm{B}} - \theta_{\pi_2})\}, \end{aligned} \tag{13}$$

and θ_{B} is the orientation of the magnetic field in the ab-plane measured from the a-axis. Then, the total magnetic energy per unit cell of this system is given by

$$E = E_{\mathrm{ex}} + E_{\mathrm{anis}} + E_{\mathrm{field}}. \tag{14}$$

We determine the most stable magnetic structure using Eq. 14. Once the angles (θ_i), which give the lowest energy (E) at a field are determined, we can directly calculate the magnetization (M) using Eq. 13. The results are shown in Fig. 11.

References

1 J. M. Williams, J. R. Ferraro, R. J. Thorn, K. D. Carlson, U. Geiser, H. H. Wang, A. M. Kini, and M.-H. Whangbo, "Organic Superconductors (Including Fullerenes); Synthesis, Structure, Properties, and Theory," Prentice Hall, Englewood Cliffs, New Jersey (1992).

2 J.-P. Farges, "Organic Conductors; Fundamentals and Applications," Marcel-Dekker Inc., New York (1994).

3 J.-I. Yamaura, K. Suzuki, Y. Kaizu, T. Enoki, K. Murata, and G. Saito, *J. Phys. Soc. Jpn.*, **65**, 2645 (1996); T. Enoki, J.-I. Yamaura, and A. Miyazaki, *Bull. Chem. Soc. Jpn.*, **70**, 2005 (1997).

4 K. Enomoto, A. Miyazaki, and T. Enoki, *Synth. Metals*, **120**, 977 (2001).

5 K. Okabe, K. Enomoto, A. Miyazaki, and T. Enoki, *Mol. Cryst. Liq. Cryst.*, **376**, 513 (2002); A. Miyazaki, M. Enomoto, K. Enomoto, J. Nishijo, T. Enoki, E. Ogura, Y. Kuwatani, and M. Iyoda, *Mol. Cryst. Liq. Cryst.*, **376**, 535 (2002).

6 S. Aonuma, H. Sawa, and R. Kato, *J. Chem. Soc., Perkin Trans. 2*, **1995**, 1541.

7 N. Hanasaki, H. Tajima, M. Matsuda, T. Naito, and T. Inabe, *Phys. Rev. B*, **62**, 5839 (2000).

8 A. Kobayashi, T. Udagawa, H. Tomita, T. Naito, and H. Kobayashi, *Chem. Lett.*, **1993**, 2179.

9 L. Brossard, R. Clerc, C. Coulon, M. Tokumoto, T. Ziman, D. K. Pertov, H. Kobayashi, and P. Cassoux, *Eur. Phys. J.*, **B1**, 439 (1998).

10 C. Hotta and H. Fukuyama, *J. Phys. Soc. Jpn.*, **69**, 2577 (2000).

11 H. Kobayashi, H. Tomita, T. Naito, A. Kobayashi, F. Sakai, T. Watanabe, and P. Cassoux, *J. Am. Chem. Soc.*, **118**, 368 (1996); H. Kobayashi, A. Kobayashi, and P. Cassoux, *Chem. Soc. Rev.*, **29**, 325 (2000).

12 S. Uji, H. Shinagawa, C. Terakura, T. Terashima, T. Yakabe, Y. Terai, M. Tokumoto, A. Kobayashi, H. Tanaka, and H. Kobayashi, *Nature (London)*, **410**, 908 (2001).

13 O. Cepas, Ross H. McKenzie, and J. Merino, *Phys. Rev. B*, **65**, 100502R (2002).

14 K. Kikuchi, T. Namiki, I. Ikemoto, and K. Kobayashi, *J. Chem. Soc., Chem. Commun.*, **1986**, 1472.

15 K. Kikuchi, K. Saito, I. Ikemoto, K. Murata, T. Ishiguro, and K. Kobayashi, *Synth. Met.*, **27**, B269 (1988); K. Kikuchi, Y. Ishikawa, K. Saito, I. Ikemoto, and K. Kobayashi, *Synth. Met.*, **27**, B391 (1988).

16 H. Yoshino, K. Saito, H. Nishikawa, K. Kikuchi, K. Kobayashi, and I. Ikemoto, *J. Phys. Soc. Jpn.*, **66**, 2410 (1997).

17 K. Kikuchi, Y. Honda, Y. Ishikawa, K. Saito, I. Ikemoto, K. Murata, H. Anzai, T. Ishiguro, and K. Kobayashi, *Solid State Commun.*, **66**, 405 (1988).

18 Y. Ishikawa, K. Saito, K. Kikuchi, K. Kobayashi, and I. Ikemoto, *Bull. Chem. Soc. Jpn.*, **64**, 212 (1991).

19 T. G. Takhirov, O. N. Karasochka, O. A. D'Yachenko, L. O. Atovmyan, M. L. Petrov, I. K. Pubtsova, and R. N. Lyubovskaya, *Zh. Strukt. Khim.*, **30**, 114 (1989).

20 H. Yoshino, K. Saito, T. Saito, H. Nishikawa, K. Kikuchi, K. Kobayashi, and I. Ikemoto, *Synth. Met.*, **96**, 19 (1998), and references therein.

21 K. Kanoda, T. Takahashi, K. Kikuchi, K. Saito, I. Ikemoto, and K. Kobayashi, *Phys. Rev. B*, **39**, 3996 (1989).

22 H. Akutsu, K. Saito, Y. Yamaura, K. Kikuchi, H. Nishikawa, I. Ikemoto, and M. Sorai, *J. Phys. Soc. Jpn.*, **68**, 1968 (1999).

23 A. C. T. North, D. C. Phillips, and F. S. Mathews, *Acta Crystallogr., Sect. A*, **24**, 351 (1968).

24 G. M. Sheldrick, "SHELXS 86, Program for the Solution of Crystal Structures," University of Göttingen, Germany (1985); G. M. Sheldrick, "SHELXL 93, Program for the Refinement of Crystal Structures," University of Göttingen, Germany (1993).

25 T. Mori, A. Kobayashi, Y. Sasaki, H. Kobayashi, G. Saito, and H. Inokuchi, *Bull. Chem. Soc. Jpn.*, **57**, 627 (1984).

26 M. Kobayashi, T. Enoki, K. Imaeda, H. Inokuchi, and G. Saito, *Phys. Rev. B*, **36**, 1457 (1987).

27 The calculated transfer integrals reported in Ref. 33 are based on the parameters in Ref. 11, which lead to too large population of HOMO on the Se atoms. Therefore, we use the new parameters suggested in Ref. 28 for this calculation.

28 T. Mori and M. Katsuhara, *J. Phys. Soc. Jpn.*, **71**, 826 (2002).

29 L. Balicas, *Phys. Rev. Lett.*, **80**, 1960 (1998); L. Balicas, *Phys. Rev. B*, **59**, 12830 (1999).

30 R. Busch, G. Ries, H. Werthner, G. Kreiselmeyer, and G. Saemann-Ischenko, *Phys. Rev. Lett.*, **69**, 522 (1992).

31 L. J. de Jongh and A. R. Miedema, *Adv. Phys.*, **23**, 1 (1974).

32 K. Sugihara, *J. Phys. Soc. Jpn.*, **62**, 624 (1993).

33 T. Enoki, T. Umeyama, A. Miyazaki, H. Nishikawa, I. Ikemoto, and K. Kikuchi, *Phys. Rev. Lett.*, **81**, 3719 (1998).

34 P. Wzietek, F. Creuzet, C. Bourbonnais, D. Jérome, K. Bechgaard, and P. Batail, *J. Phys. I*, **3**, 171 (1993).

35 M. Dumm, A. Loidl, B. W. Fravel, K. P. Starkey, L. K. Montgomery, and M. Dressel, *Phys. Rev. B*, **61**, 511 (2000); M. Dumm, A. Loidl, B. Alavi, K. P. Starkey, L. K. Montgomery, and M. Dressel, *Phys. Rev. B*, **62**, 6512 (2000).

36 R. J. Elliott, *Phys. Rev.*, **96**, 266 (1954).

37 K. Mortensen, Y. Tomkiewicz, T. D. Schultz, and E. M. Engler, *Phys. Rev. Lett.*, **46**, 1234 (1981); K. Mortensen, Y. Tomkiewicz, and K. Bechgaard, *Phys. Rev. B*, **25**, 3319 (1982).

38 G. Grüner, *Rev. Mod. Phys.*, **66**, 1 (1994).

39 T. Nakamura, T. Nobutoki, Y. Kobayashi, T. Takahashi, and G. Saito, *Synth. Metals*, **70**, 1293 (1995).

40 K. Enomoto, A. Miyazaki, and T. Enoki, in preparation.

41 Y. Meir, *Phys. Rev. Lett.*, **83**, 3506 (1999).